REGIONAL-SCALE DIFFERENTIAL TIME TOMOGRAPHY METHODS: DEVELOPMENT AND APPLICATION TO THE SIBERIA DATA SET

Haijiang Zhang[1, 2], Kevin G. Mackey[3], Kazuya Fujita[3], Clifford H. Thurber[1], Lee K. Steck[4], Charlotte A. Rowe[4], Steven Roecker[5], and M. Nafi Toksoz[2]

University of Wisconsin-Madison[1], Massachusetts Institute of Technology[2], Michigan State University[3], Los Alamos National Laboratory[4], and Rensselaer Polytechnic Institute[5]

Sponsored by the National Nuclear Security Administration

Award No. DE-FC52-06NA27325
Proposal No. BAA06-77

ABSTRACT

This is the final year of a collaborative project by the University of Wisconsin-Madison (UW-Madison), Massachusetts Institute of Technology (MIT), Michigan State University (MSU), and Los Alamos National Laboratory (LANL). There are four main tasks in this project: (1) an extension of our development of double-difference (DD) seismic tomography to the use of station-pair residual differences, including incorporation of a new method for resolution matrix calculation; (2) testing, refinement, and adaptation of a method for spherical-earth finite-difference (SEFD) travel time calculations for use in DD tomography; (3) an extension of our Cartesian adaptive-grid DD tomography algorithm to spherical coordinates; and (4) collaborative work among the UW-Madison, MIT, MSU, and LANL groups to apply these analysis tools to the Siberia data set.

As reported in previous Monitoring Research Review proceedings, we have successfully incorporated station-pair differential times into the extended DD tomography code. A new resolution matrix calculation method based on the PROPACK package is also incorporated and tested, which is able to efficiently and accurately estimate singular values and vectors for large matrices based on the Lanczos bidiagonalization with partial reorthogonalization. In our tomography algorithm, we use a spherical-Earth finite-difference (SEFD) travel time method to calculate travel times and trace rays. The basic concept is the extension of a standard Cartesian FD travel time algorithm to the spherical case through development of a mesh in radius, co-latitude, and longitude, expression of the finite difference (FD) derivatives in a form appropriate to the spherical mesh, and the construction of “stencils” to calculate extrapolated travel times. We benchmarked the SEFD method against the “sphere-in-a-box” Cartesian FD travel time algorithm (Flanagan et al., 2007). We have applied the extended DD tomography algorithm separately to the southern (Baikal and Amur regions) and northern (Magadan and eastern Yakutsk regions) parts of the eastern Siberia. The velocity models in both parts show strong heterogeneities at shallow depths, as expected for the variable and complicated nature of the crust.

For this last year, we focus our effort on extending the spherical regular-grid DD tomography code to the adaptive version, in which the inversion grid nodes are adapted according to the data distribution. In addition to the data we already collected for the Baikal, Amur, Magadan and Yakutsk regions, we also collect the data for the Kamchatka region. We first apply the spherical regular-grid DD tomography method to the whole data set to obtain a seamless velocity model for eastern Siberia. The adaptive-grid DD tomography method will also be applied to the whole data set. The model will be tested using the peaceful nuclear explosions (PNEs) that occurred and were recorded in the region.

OBJECTIVES

The objectives of this project are to investigate and develop new and improved methodologies for regional-scale three-dimensional (3D) seismic tomography using a combination of event- and station-pair arrival time differences, and to apply the new methods to the MSU and LANL Siberia database. The tomographic work proposed here will provide a more reliable velocity model for both the crust and upper mantle of eastern Siberia. There are four main tasks in this project: (1) an extension of our development of double-difference (DD) seismic tomography to the use of station-pair residual differences, including the incorporation of a new method for resolution matrix calculation; (2) testing, refinement, and adaptation of a method for SEFD travel time calculations for use in DD tomography; (3) an extension of our Cartesian adaptive-grid DD tomography algorithm to spherical coordinates; and (4) collaborative work among the UW-Madison, LANL, and MSU groups to apply these analysis tools to the Siberia data set. In the last year of this project, our focus is to assemble a data set for the whole eastern Siberia region and determine both the 3D *P*- and *S*-wave velocity models.

RESEARCH ACCOMPLISHED

Tectonic Setting

Eastern Russia is composed of a series of allochthonous terranes that have accreted to the Precambrian Siberian (North Asian) craton (Figure 1). In the southern part (Baikal and Amur regions), terranes form a suture zone between the Siberian and North China cratons. The terranes vary in age, but a large majority of them accreted in the Mesozoic and Cenozoic. Superimposed on the Meso-Cenozoic accretionary complex is the present-day plate boundary system between the Eurasian, North American, and Pacific plates (Figure 2). The complexities of intracontinental deformation have resulted in the development of several microplates (or blocks) and broad zones of deformation. In addition to compressional features that dominate continental northeast Asia, there are extensive areas of Late Cenozoic coastal sediments and, in parts of the Russian Northeast and in Baikal, active and Cenozoic rift systems (Fujita et al., 1997).

The present-day plate boundaries are a result of the interaction of the North American, Eurasian, and Pacific plates. In northeastern Russia, the Arctic Mid-Ocean rift (Figure 2) propagates into the Asian continent in the Laptev Sea. Active rifting has been documented through focal mechanism studies (e.g., Fujita et al., 1990) and seismic reflection profiling (Drachev et al., 1998) through the Laptev Sea, up to the southern end of Bour Khaya Gulf. This tectonic evolution has created a very heterogenous crust, ranging from old Precambrian shields to young areas of active rifting. This heterogeneity should be reflected in both the crustal and upper mantle structure of the region, which can be identified through tomographic modeling

Data Collection and Quality Control

We have assembled a data set for the eastern Siberia region in the area of 40^{o} to 75^{o} latitude and 100^{o} to 175^{o} longitude for the period of 1977 to 2007 from the MSU and LANL Siberia database. There are ~228,000 *P* (*Pg*+*Pn*) and ~231,000 S (*Sg*+*Sn*) phases corresponding to ~28000 events and ~290 stations. For each event, there are at least 5 observations. Figure 3 shows composite travel curves for *Pg* and *Sg* and first *P* and *S* arrivals, respectively. From the travel time curves shown in Figure 3, we note there are some outliers in the catalog picks. We cleaned up the *P* and *S* times by removing outliers falling outside the major trend of the travel time curves (indicated by green bands for *Pg*+*Sg* and red bands for first *P*+*S* arrivals). As a result, we obtained ~190,000 first *P* and ~160,000 first *S* arrivals. In comparison, there are ~46,000 Pg and ~81,000 Sg times. In this paper, we only report on the seismic tomography study using the first *P* and *S* arrivals.

Model Resolution Analysis

For a linear inverse problem with *m* observations and *n* model parameters, the singular value decomposition (SVD) of the *m* by *n* sensitivity matrix **A** is

$$\mathbf{A} = \mathbf{U}\mathbf{S}\mathbf{V}^{\mathrm{T}} = \sum_{i=1}^{n} s_i \mathbf{u}_i \mathbf{v}_i^{\mathrm{T}} , \tag{1}$$

where the matrices $\mathbf{U} \in \mathrm{R}^{m\times m}$ and $\mathbf{V} \in \mathrm{R}^{n\times n}$ are orthogonal and **S** is an *m* by *n* diagonal matrix with nonnegative diagonal elements called singular values. The singular values are generally arranged in decreasing size (Aster et al., 2005).

If only the first p nonzero singular values are chosen, the truncated SVD of **A** is

$$\mathbf{A} = \mathbf{U}_\mathrm{p}\mathbf{S}_\mathrm{p}\mathbf{V}_\mathrm{p}^\mathrm{T} = \sum_{\mathrm{i=1}}^{\mathrm{p}} s_\mathrm{i}\mathbf{u}_\mathrm{i}\mathbf{v}_\mathrm{i}^\mathrm{T} \,. \tag{2}$$

The pseudoinverse of **A** is then given by

$$\mathbf{A}^{-1} = \mathbf{V}_\mathrm{p}\mathbf{S}_\mathrm{p}^{-1}\mathbf{U}_\mathrm{p}^\mathrm{T} \,. \tag{3}$$

The resolution matrix **R** is represented as

$$\mathbf{R} = \mathbf{A}^{-1}\mathbf{A} = (\mathbf{A}^\mathrm{T}\mathbf{A})^{-1}\mathbf{A}^\mathrm{T}\mathbf{A} = \mathbf{V}_\mathrm{p}\mathbf{V}_\mathrm{p}^\mathrm{T} , \tag{4}$$

which acts as a filter between the true and inverted model parameters.

Because of the noise in the data and ill-conditioning of the system, it is typically necessary to use some regularization methods to stabilize the inverse system. Suppose the regularization operator is **L**, then the regularized inverse of **A** is

$$\mathbf{A}^{-} = (\mathbf{A}^\mathrm{T}\mathbf{A} + \alpha^2\mathbf{L}^\mathrm{T}\mathbf{L})^{-1}\mathbf{A}^\mathrm{T} \,. \tag{5}$$

The most common regularization tool is damping, or zeroth-order Tikhonov regularization (Aster et al., 2005). Assuming the damping factor is λ, the pseudoinverse of **A** in this case is defined as

$$\mathbf{A}^{-} = \mathbf{V}\mathbf{S}^{-1}\mathbf{D}\mathbf{U}^\mathrm{T} , \tag{6}$$

where **D** is a diagonal matrix defined as

$$\mathbf{D} = \frac{\mathbf{S}^2}{\mathbf{S}^2 + \lambda^2\mathbf{I}} \,. \tag{7}$$

In the case of using other non-diagonal regularization methods such as first-order or second-order smoothing constraints, there is no simple way equivalent to Equation (6) to represent the pseudo-inverse of the matrix **A**, although the generalized SVD can be used to develop a similar representation (Aster et al., 2005). Suppose the SVD of the augmented matrix $\mathbf{B} = \begin{bmatrix} \mathbf{A} \\ \alpha\mathbf{L} \end{bmatrix}$ is defined as $\mathbf{B}=\mathbf{QP\Lambda}^\mathrm{T}$. The resolution matrix **R** in this case is equal to

$$\mathbf{R} = \mathbf{Q\Sigma Q}^\mathrm{T} , \tag{8}$$

where $\mathbf{\Sigma}$ is given by $\mathbf{\Sigma} = \mathbf{I} - \mathbf{\Lambda}^{-1}(\mathbf{P}_2)^\mathrm{T}(\mathbf{P}_2)\mathbf{\Lambda}$ and $\mathbf{P}_2$ is the submatrix of **P** corresponding to the *Nr* rows of the smoothing constraints (Vasco et al., 2003). In many cases, one also includes damping in addition to the smoothing constraints. In this case $\mathbf{\Sigma}$ is given by

$$\mathbf{\Sigma} = \mathbf{D\Lambda}^{-1}\left(\mathbf{I} - (\mathbf{P}_2)^\mathrm{T}(\mathbf{P}_2)\right)\mathbf{\Lambda} \tag{9}$$

Recently, a package called PROPACK that can accurately estimate the singular values and vectors for sparse matrices was developed by Larsen (1998). The PROPACK package is based on the Lanczos bidiagonalization process but it is able to estimate the larger singular values and vectors more accurately. We integrate the PROPACK package into the spherical-earth double-difference seismic tomography code *tomoSPDD* to estimate model resolution and covariance matrices for various problem sizes, similar to what was done with *tomoDD* (Zhang and Thurber, 2007). This method is shown to be very efficient for estimating the full model resolution matrix for inverse problems having hundreds of thousands of observations and tens of thousands of model parameters. Using this method, estimating the full model resolution matrix is no longer a significant challenge for large inverse problems.

Determining the Velocity Model for the Eastern Siberia

We noticed that in the selected data base of first arrivals, many events actually lie in the Kamchatka region. We decimated events in the Kamchatka region by selecting those having the maximum number of phases in a 3D grid of 0.05° in latitude by 0.2° in longitude and by 1 km in depth. As a result, the number of events decreases from 19250 to 9513. In total, there are 109000 P and 87800 S phases selected on 257 stations (Figure 4). The inversion grid intervals are 1° in latitude and 2° in longitude. In depth, the grid nodes are positioned at 0, 15, 30, 35, 45, 75, and 115 km. Because of the large grid intervals, we only used the absolute arrivals in the spherical double-difference tomography code *tomoSPDD*, in which a spherical pseudo-bending ray tracing algorithm is adopted. We started the inversion from a 1D Vp velocity model with a constant Vp/Vs ratio of 1.732. Both smoothing and damping regularization methods are used to make the tomograhic system stable. The optimal smoothing weight and damping parameters are selected through a trade-off analysis of model variance and data variance. The initial travel time residuals show a skewed distribution centered around 2 s (Figure 5). After 5 simultaneous inversions, the travel time residuals have a Gaussian-like distribution (Figure 5), indicating the systematic errors in seismic event locations and velocity model are corrected. The unweighted root-mean-square (RMS) residual reduces from 2.927 s to 0.607 s. The model resolution is assessed using the diagonal values of the resolution matrix, calculated using PROPACK (Figure 6). Considering the smoothing, regions with resolution values greater than 0.2 are expected to be relatively well resolved.

The crustal Vp and Vs models (Z = 0 and 15 km of Figures 7 and 8) generally reflect many Cenozoic tectonic features and are in general agreement with previous studies. There are low velocities below the presently active Kamchatka volcanic arc. Sakhalin has low crustal velocities (Vp ~ 5.8-6.0 km/sec, Vs ~ 3.3-3.4 km/sec) as also determined by Mackey et al. (2003) and Steck et al. (2009). The shallow region under the Baikal rift has slightly elevated Vp and Vs, as noted by Mackey et al. (2003) and in Soviet long-range refraction profiles (e.g., Pavlenkova et al., 2002). Unfortunately, our results do not extend into the Siberian platform or outside the Chersky Seismic Belt (CSB) at shallow depths, thus we are unable to determine whether the CSB has a lower velocity than adjacent areas. Like other studies, there is insufficient resolution to determine if the crustal seismic velocities determined here reflect the accretionary history of the region in detail (Figures 1, 7, and 8).

The upper mantle slices (Z = 35-115 km of Figures 7 and 8), show lower velocities under the Baikal rift zone and extending under the basins to the northeast (e.g., Gao et al., 1994) and, possibly, eastwards towards Sakhalin as well. In Kamchatka, the low velocities appear to persist to a depth of about 100 km, presumably reflecting the mantle wedge and partial melting above the subducting lithosphere.

Lower velocities also appear to exist at both shallow and deeper depths in various parts of the CSB and near the coast of the Arctic Ocean. The former may reflect rifting in the presumed post-Pliocene Moma rift episode (e.g., Fujita et al., 1990) or widespread plume-like activity as suggested by Grachev (2003). In the 15 km depth slice of the Vp model (Figure 7), low velocities near 63°N, 135-140°E are close to a region of thin crust (Mackey et al., 1998) with elevated heat flow (Parfenov et al., 1988). The latter correlates with the southernmost extent of extension associated with the Arctic (Gakkel) mid-ocean ridge.

CONCLUSIONS AND RECOMMENDATIONS

We assembled a dataset for eastern Siberia comprising *Pn*+*Pg* and *Sn*+*Sg* picks. A spherical regular-grid double-difference tomography code *tomoSPDD* is applied to the assembled first *P* and *S* arrivals to obtain both Vp and Vs models of eastern Siberia. The PROPACK package is incorporated into the code to estimate the model resolution matrix based on the Lanczos bidiagonalization with partial reorthogonalization. The velocity model shows good correlation with the local geological settings and other studies. We plan to use the adaptive inversion mesh based on tetrahedral diagrams according to the data coverage to further refine the velocity model. We will also test it using the PNEs that occurred and were recorded in the region.

REFERENCES

Aster, R.C., B. Borchers, and C. H. Thurber (2005). *Parameter estimation and inverse problems*, Elsevier Academic Press, Burlington, MA, 301 pp.

Drachev, S. S., L. A. Savostin, V. G. Groshev, and I. E. Bruni (1998). Structure and geology of the continental shelf of the Laptev Sea, eastern Russian Arctic, *Tectonophysics* 298: 357–393.

Fujita, K., F. W. Cambray, and M. A. Velbel (1990). Tectonics of the Laptev Sea and Moma rift systems, northeastern USSR, *Mar. Geol.* 93: 95-118.

Fujita, K., D. B. Stone, P. W. Layer, L. M. Parfenov, and B. M. Koz'min (1997). Cooperative program helps decipher tectonics of northeastern Russia: *Transactions of the American Geophysical Union (Eos)* 78: 245, 252–253.

Flanagan, M. P., S. C. Myers, and K. D. Koper (2007). Regional travel-time uncertainty and seismic location improvement using a three-dimensional *a priori* velocity model, *Bull. Seism. Soc. Am.* 97: 804–825.

Grachev, A. F. (2003). The Arctic rift system and the boundary between the Eurasian and North American lithospheric plates: New insight to plate tectonic theory, *Russ. J. Earth Sc.* 5: 307–345.

Gao , S., P. M. Davis, H. Liu, P. D. Slack, Y. A. Zorin, N. A. Logatchev, M. Kogan, P. D. Burkholder, and R. P. Meyer (1994). Asymmetric upwarp of the asthenosphere beneath the Baikal rift zone, Siberia, *J. Geophys. Res.* 99: 15319–15330.

Larsen, R. M. (1998). Lanczos bidiagonalization with partial reorthogonalization, Department of Computer Science, Aarhus University, Technical Report, DAIMI PB-357, September 1998. The PROPACK package realizing this algorithm is available at http://soi.stanford.edu/~rmunk/PROPACK/.

Mackey, K. G., K. Fujita, and L. J. Ruff (1998). The crustal thickness of northeast Russia, *Tectonophysics* 284: 283–297.

Mackey, K. G., K. Fujita, L. K. Steck, and H. E. Hartse (2003). Seismic Regionalization in Eastern Russia, in *Proceedings of the 25th Seismic Research Review—Nuclear Explosion Monitoring: Building the Knowledge Base,* LA-UR-03-6029, Vol. 1, pp. 73–82.

Parfenov, L. M., B. M. Koz'min, O. V. Grinenko, V. S. Imaev, and L. P. Imaeva (1988). Geodynamics of the Chersky seismic belt, *J. Geodyn.* 9: 15–37.

Pavlenkova, G. A., K. Priestley, and J. Cipar (2002). 2D model of the crust and uppermost mantle along RIFT profile, Siberian craton, *Tectonophysics* 355: 171–186.

Steck, L. K., W. S. Philips, K. Mackey, M. L. Begnaud, R. J. Stead, and C. A. Rowe (2009). Seismic tomography of crustal *P* and *S* across Eurasia, *Geophys J. Int.* 177: 81–92.

Vasco, D.W., L. R. Johnson, and O. Marques (2003). Resolution, uncertainty, and whole Earth tomography, *J. Geophys. Res.* 108: (B1), 2022.

Zhang, H. and C. H. Thurber (2007). Estimating the model resolution matrix for large-seismic tomography problems based on Lanczos bidiagonalization with partial reorthogonalization, *Geophys. J. Int.* 170: 337–345.

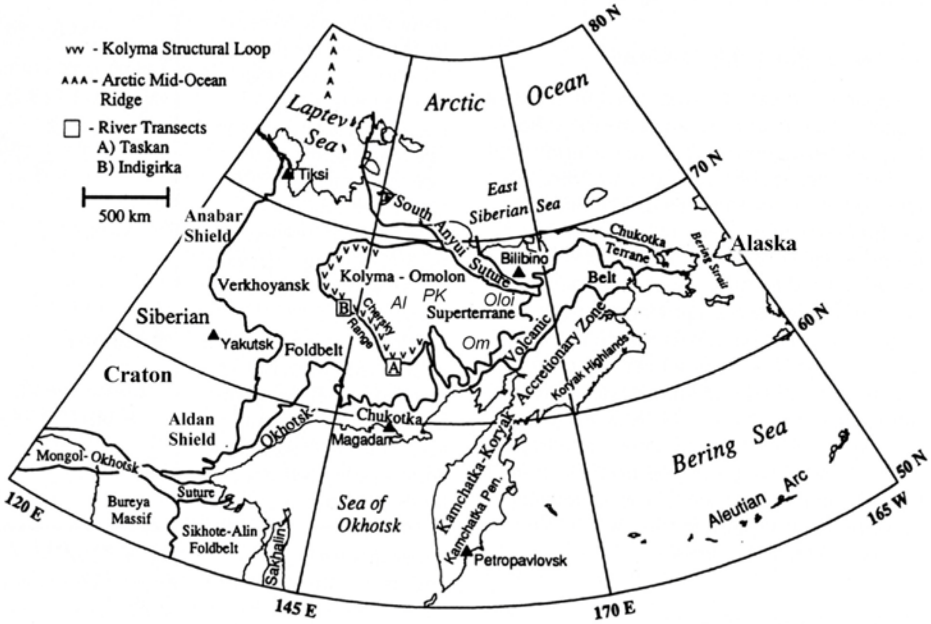

Figure 1. Geologic index map of northeastern Russia showing major tectonic provinces. The Arctic Mid-Ocean Ridge is shown by inverted v's, the Kolyma structural loop of Zonenshain *et al*. (1990) is shown by v's. Global seismic network stations are shown by triangles. River transects conducted by the University of Alaska (transect B also in conjunction with Michigan State University) are shown by lettered boxes. Abbreviations: Al – Alazeya arc, PK – Prikolyma terrane, Om – Omolon terrane, Oloi – Oloi arc. Figure adapted from Fujita *et al*. (1997).

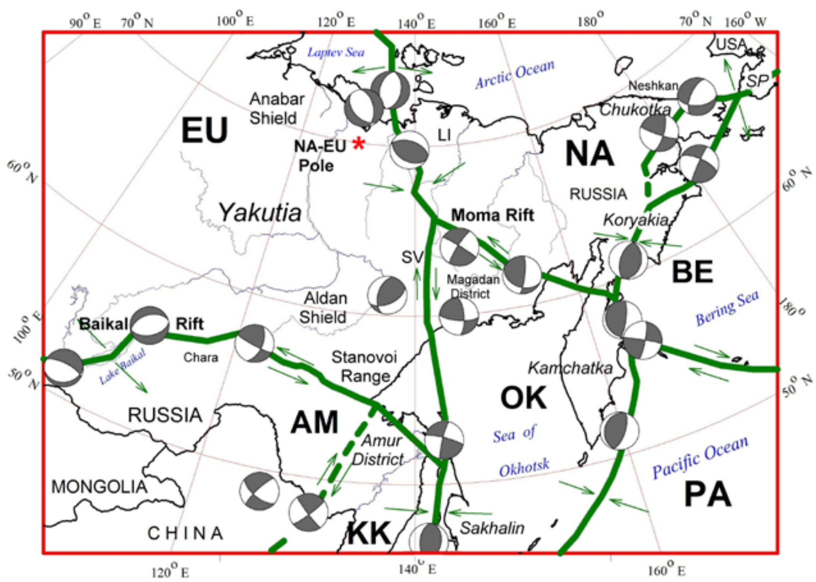

Figure 2. Present-day tectonic map of eastern Russia showing major plate and block boundaries, representative focal mechanisms, and localities and features discussed in the text. Arrows show directions of relative movement. Plate boundaries shown in green (dashed where speculative or uncertain). The red asterisk shows the approximate location of the North America – Eurasia (NA-EU) Euler pole of rotation. Plate and block abbreviations: EU – Eurasia, NA – North America, PA – Pacific, AM – Amur, OK – Okhotsk, BE – Bering, and KK – Korea-Khabarovsk. Other abbreviations: LI – Lower Indigirka rift zone, SV – South Verkhoyansk district, SP – Seward Peninsula.

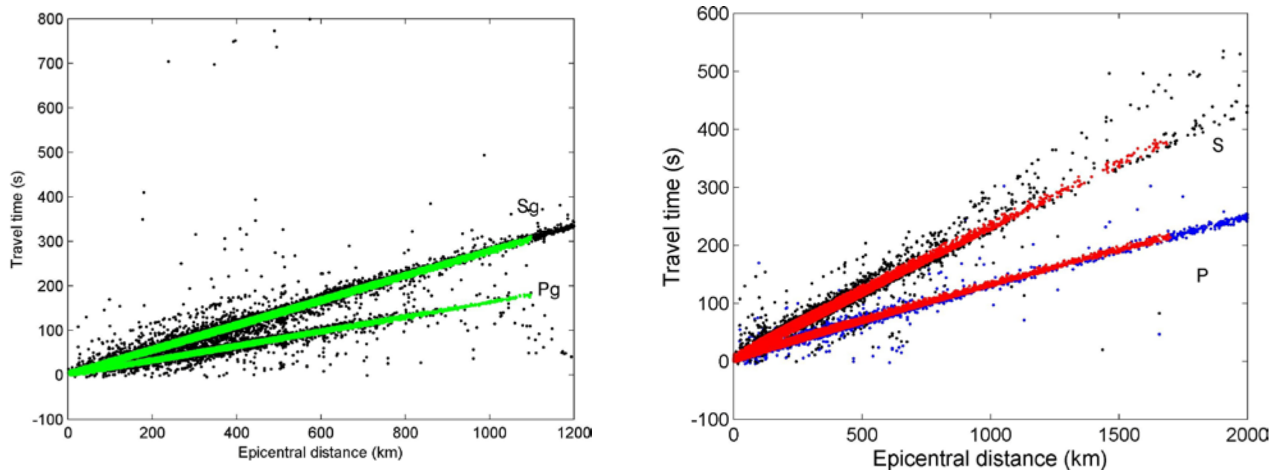

Figure 3. Travel time curves for (left) Pg and Sg phases and (right) first P and S phases. Green lines represent selected Pg and Sg phases and red lines indicate selected first P and S arrivals.

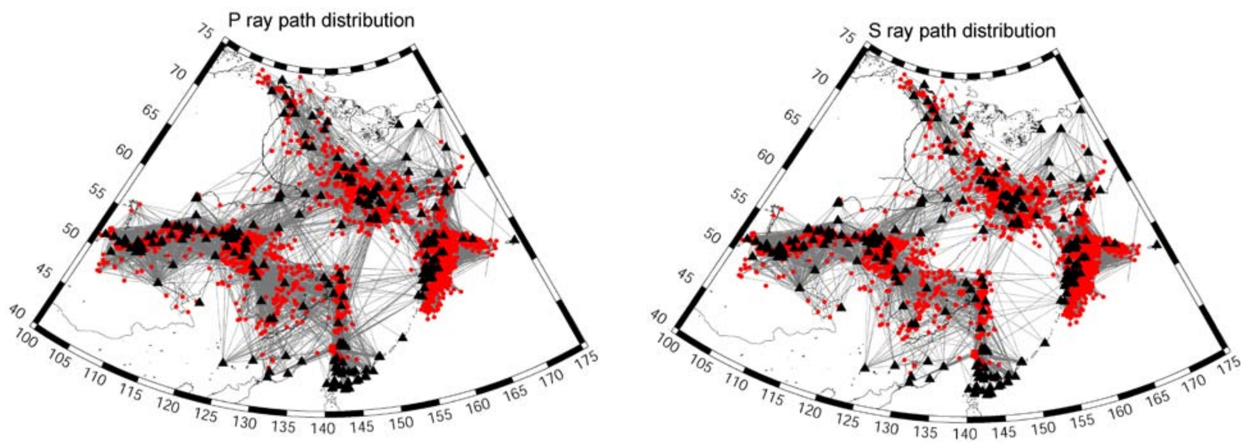

Figure 4. *P* and *S* ray path distributions for selected P and S first arrivals. Earthquakes are red dots and black triangles are stations.

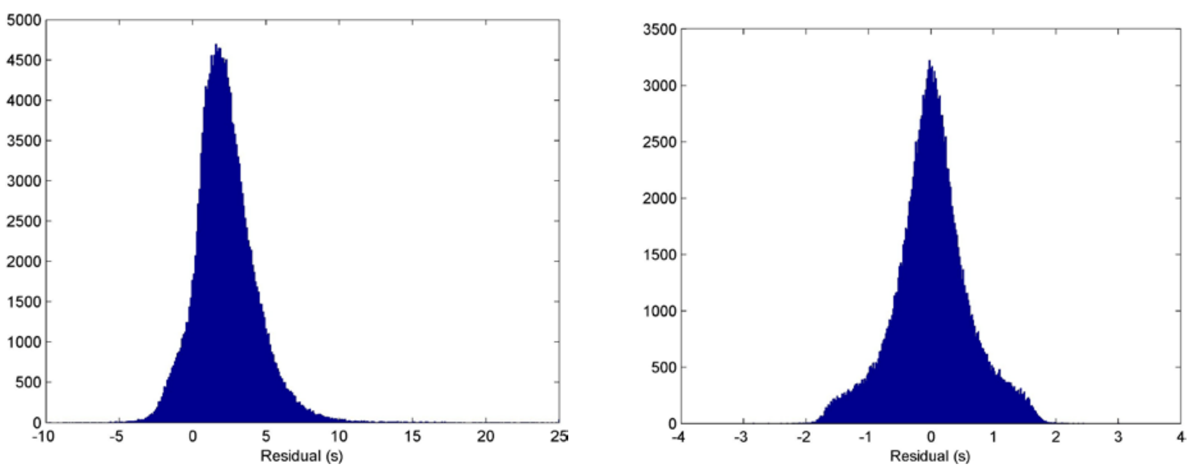

Figure 5. Comparison of histograms of travel time residuals (left) before and (right) after seismic tomography.

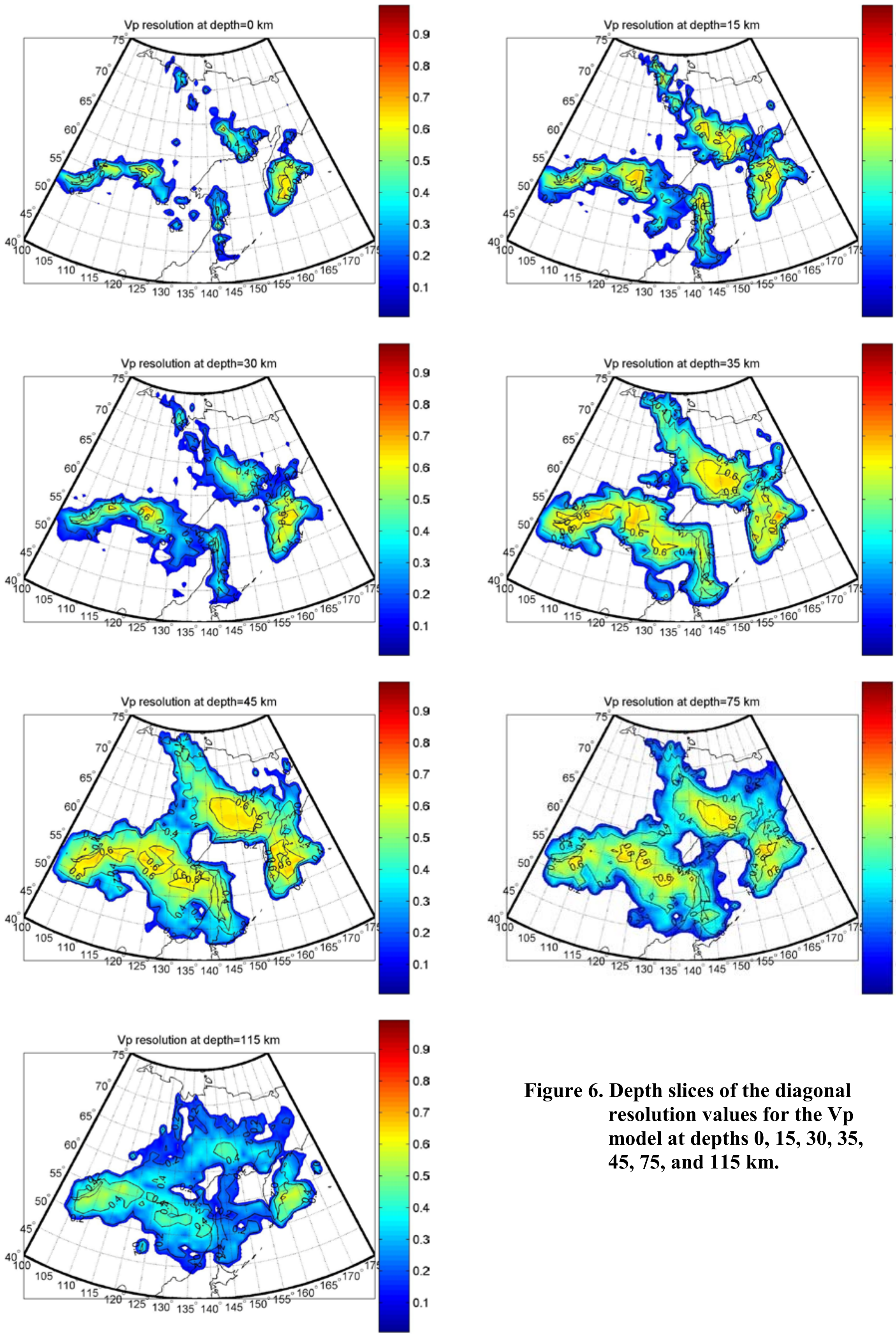

Figure 6. Depth slices of the diagonal resolution values for the Vp model at depths 0, 15, 30, 35, 45, 75, and 115 km.

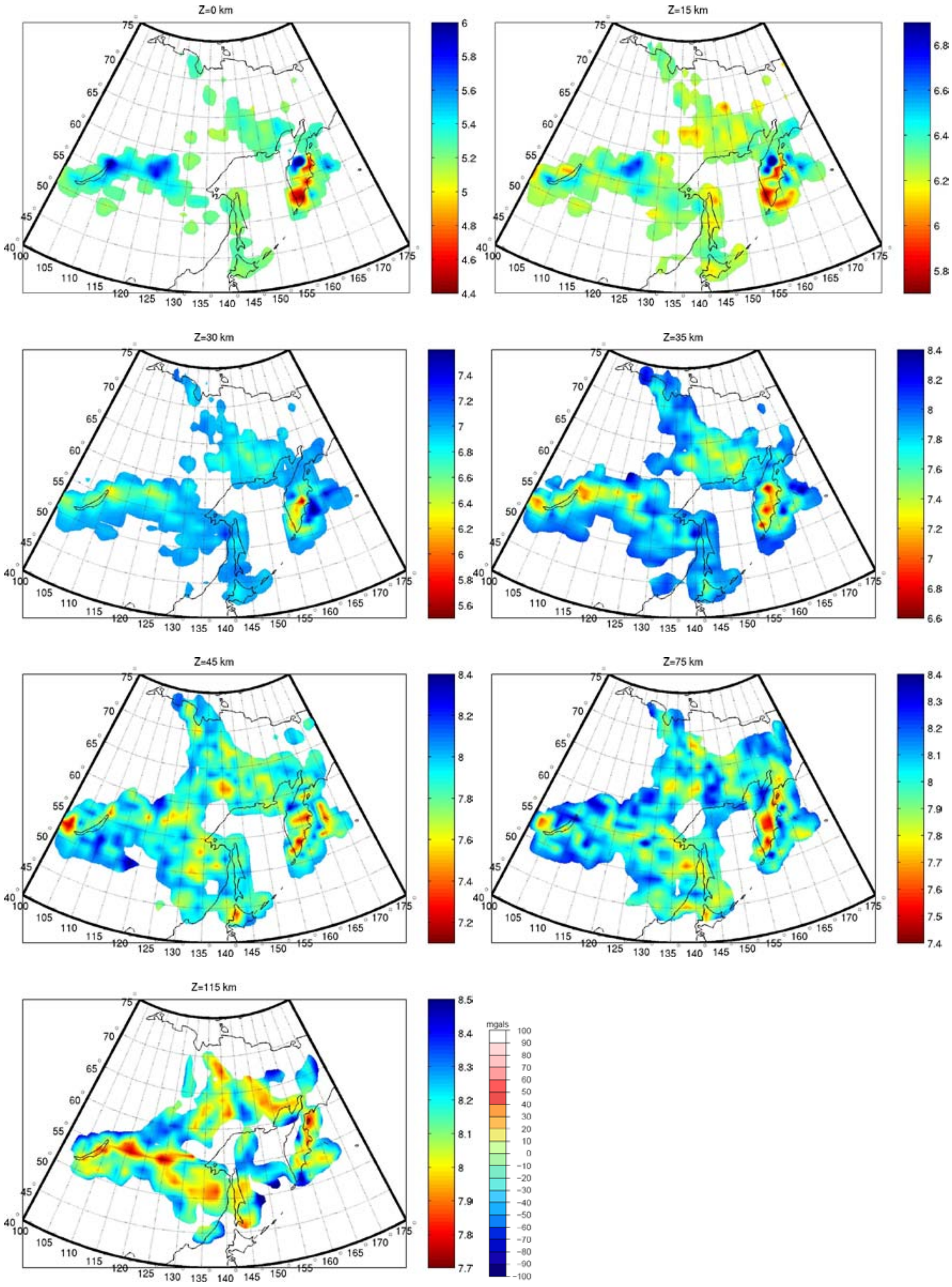

Figure 7. Depth slices of the Vp model at depths 0, 15, 30, 35, 45, 75, and 115 km.

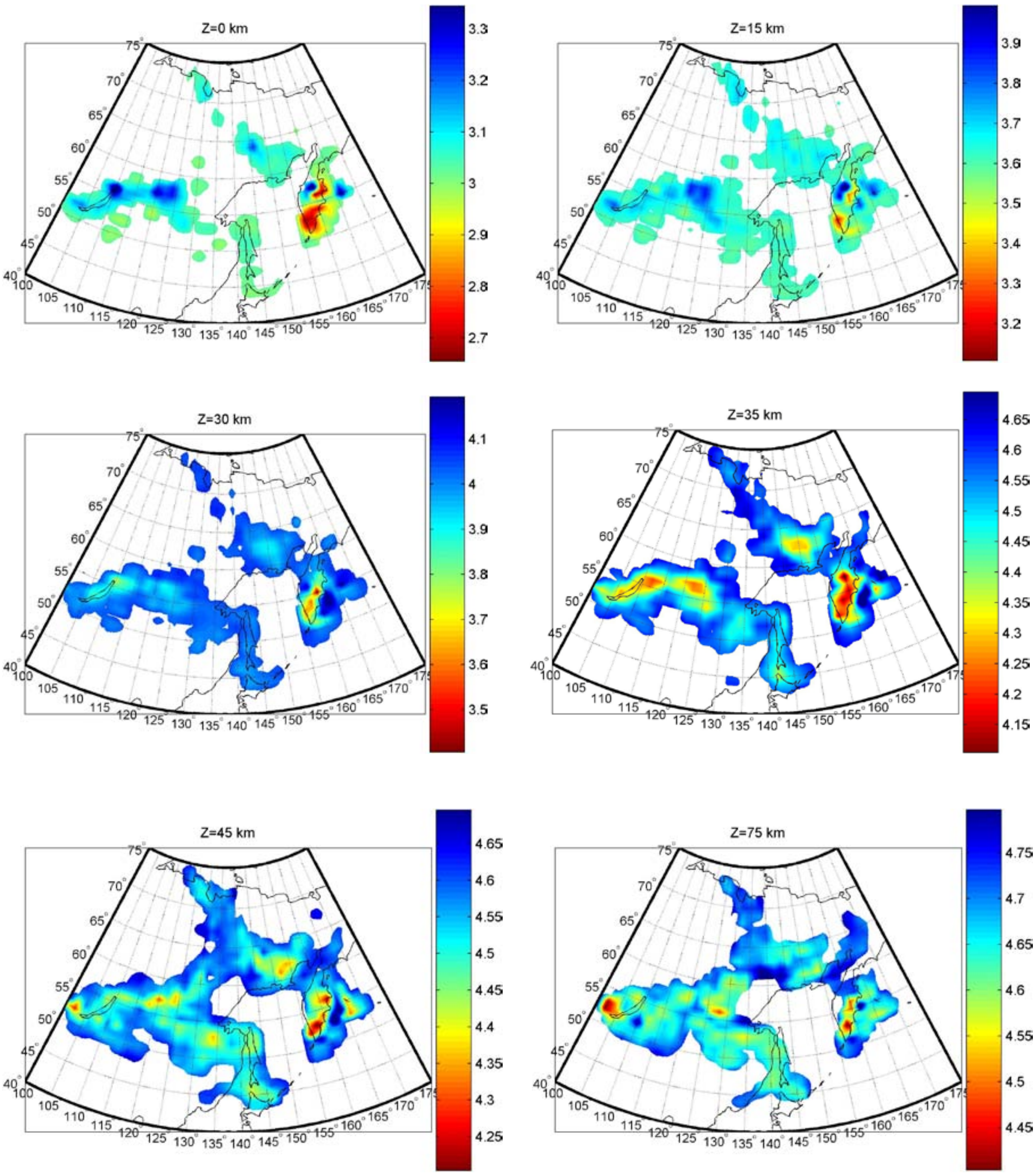

Figure 8. Depth slices of the Vs model at depths 0, 15, 30, 35, 45 and 75 km.